New Journal of Physics
The open access journal at the forefront of physics

Deutsche Physikalische Gesellschaft DPG IOP Institute of Physics International Year of Quantum Science and Technology

ACCEPTED MANUSCRIPT • OPEN ACCESS

Enhancing Local Ionization in Micro-Gap Atmospheric Discharge

To cite this article before publication: Yize Liu *et al* 2025 *New J. Phys.* in press https://doi.org/10.1088/1367-2630/adee3f

Enhancing Local Ionization in Micro-Gap Atmospheric Discharge

Yize Liu*[1,2], Nicolas Le Thomas[2,3], Christophe Leys[1], and Anton Nikiforov[1]

[1] Research Unit Plasma Technology (RUPT), Department of Applied Physics, Faculty of Engineering and Architecture, Ghent University, St-Pietersnieuwstraat 41 B4, 9000 Ghent, Belgium

[2]Photonics Research Group, INTEC Department, Ghent University-imec, Technologiepark Zwijnaarde 126, 9052 Ghent, Belgium

[3]Center for Nano- and Biophotonics, Ghent University, Technologiepark Zwijnaarde 15, 9052 Ghent, Belgium

June 27, 2025

Abstract

Enhancement of local ionization in micro-gap atmospheric dielectric barrier discharges (DBD) is achieved experimentally via spatiotemporal control combining geometric confinement and harmonic excitation, namely adding a second-order harmonic to the applied voltage. Optimizing plasma emission near the dielectric surface is proposed as a possible route for ultraviolet plasma-on-chip sources (UV-POCS). This approach aims to overcome the lack of integrated UV sources compatible with photonic integrated circuits (PICs). Reducing the discharge gap down to 100 µm intensifies near-chip ionization and emission by enhancing the sheath electric field and sheath overlapping during polarity reversal. Harmonic excitation, especially with a 270° phase difference, amplifies peak gap voltages, redistributing power temporally to further enhance local ionization and emission on the chip surface. Experiments show 48% enhancement in surface emission with the combined techniques, alongside emission profile transitions from multi-layer to single-zone structures as the gap reduces. A 1D plasma model is presented to provide insight into emission characteristics and sheath dynamics, confirming spatiotemporal control of the electric field as a prospective strategy for enhancing surface ionization and efficiently coupling UV plasma emission into PICs.

Keywords— atmospheric pressure plasma, dielectric barrier discharge, harmonic excitation, enhanced ionization

1 Introduction

The ultraviolet (UV) spectrum offers interesting opportunities for biological and chemical sensing applications, as numerous molecules, including proteins and nucleic acids, exhibit significant absorption in this wavelength range [1]. However, the impact of this wavelength range remains limited. The main reason is the difficulty of producing, guiding, and shaping UV light efficiently. Significant progress has recently been made in guiding and shaping UV light through the development of new photonic integrated circuits (PICs) made of alumina and silica materials, operating in the UV-A and UV-C ranges, respectively [2, 3, 4]. PICs have the advantage of controlling light compactly and cost-effectively, and they can be mass-produced. In light of recent advances, the primary bottleneck preventing the widespread deployment of UV photonic sensors is the UV light source, where microplasma discharges may offer a potential solution.

UV sources are currently either coherent light sources that are bulky, expensive, or inefficient in terms of power consumption, such as excimer lasers or frequency-quadrupled laser sources based on nonlinear crystals, or incoherent broadband extended sources such as light-emitting diodes (LED) or xenon-, mercury-, or deuterium-based plasma lamps that enable the collection of only a few femtowatts of power inside a single-mode waveguide. Collecting coherent light and, even more, incoherent light in a single-mode waveguide is essential in high-performance spectroscopic or imaging applications. However, coupling the emission of an extended incoherent light source from the far field into a waveguide is of very low efficiency due to fundamental optical reasons, namely the conservation of the étendue. To overcome this problem, we suggest to locate the source in the evanescent field of a waveguide

*Corresponding author. email: Yize.Liu@UGent.be

that has a high index contrast between its core and the cladding part and propagation losses as low as possible to capture the emission over very long distances. Plasma of electrical discharges is a priori a promising candidate for such an approach in view of unique physical properties. First, plasma can emit UV light with a very large spectral bandwidth from the deep UV region below 100 nm to the deep infrared range. Second, it can be part of the low-index cladding. Critically, the low refractive index of the plasma at the emitted wavelength has a negligible impact on the waveguide properties. Finally, the conversion efficiency from electric current to UV light can be as large as 20% in plasma [5].

The primary challenge lies in the significant dimensional disparity between the plasma's emission region and the waveguide's evanescent coupling zone. The former is characterized by a Debye sheath (transitioning from plasma bulk to solid wall) that spans tens of microns, within which emission intensity decays exponentially. The latter, which envelops the waveguide, however, is within 3 µm from the chip surface (see Fig. 1).

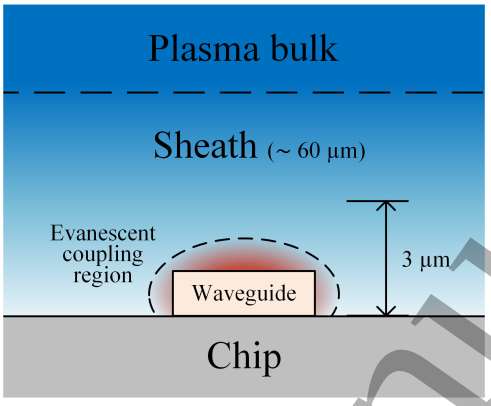

Figure 1: Schematic of evanescent plasma-waveguide coupling.

The purpose of this paper is to quantify the UV emission rate of the microplasma in the evanescent field of a waveguide and investigate the optimal plasma conditions to enhance the coupling efficiency of light. We focus here on the UV-emitting (mainly UVA) dielectric barrier discharge (DBD) plasma on top of the chip, which we call ultraviolet plasma-on-chip source (UV-POCS) in short. The photonic chip serves as the dielectric barrier and the top electrode is a metallic tip. The micro-gap on-chip plasma can be sustained with an electronic integrated circuit inside an encapsulation [6] filled with a mixture of helium and nitrogen at atmospheric pressure. To ensure a substantial number of photons are coupled evanescently into the waveguide, a sufficient density of emitters must be present near the waveguide. Since the emitters originally gain energy from electrons, the local ionization at the chip surface needs to be enhanced, which requires a thorough understanding of the DBD microplasma.

DBD, first described by Siemens in 1857 [7], is a classical low-temperature plasma configuration that features at least one layer of dielectric between two electrodes (in UV-POCS the chip serves as the dielectric barrier), widely used in industry for its ability to produce reactive species and UV emission [8]. The atmospheric micro-gap DBD plasma is well suited for realizing UV-POCS because the atmospheric pressure ensures a uniform discharge (diffuse DBD [9, 10]) and a high electron-neutral collision rate, minimizing sheath thickness, while the micro-gap configuration aligns with the requirements for miniaturization. Compared to conventional DBD geometries (with a discharge gap on the order of mm) that have been well characterized, micro-gap configurations (< 500 µm) remain less explored. The high electric field in the microscale gap can lead to different patterns of space charge [11] and discharge mode transitions [12] compared to those observed in larger gaps. In this sense, optimization of the gap spacing can result in a direct enhancement of the discharge. In addition to enhancing the electric field spatially, voltage waveform tailoring, specifically harmonic excitation, has been shown to induce localized discharge enhancement in radio frequency plasma [13] and in DBD [14].

In this paper, we experimentally and numerically investigate the enhancement of local ionization and UV emission in a micro-gap atmospheric plasma near the dielectric surface of a photonic chip by controlling the geometric confinement and the use of harmonic excitation. A 1D plasma model is developed to provide insight into the ionization enhancement mechanism under controlled external conditions. The paper is organized as follows. Section 2 describes the experimental setup and modeling framework, including pre-test results that determine a baseline operation condition used in both the experiment and simulation. Section 3 explores the impact of discharge gap spacing on ionization dynamics, with Subsection 3.1 presenting the variation of measured emission intensity profiles along the gap spacing (80-400 µm), and Subsection 3.2 providing theoretical interpretations through time-averaged and time-sampling analyses. Section 4 further examines the harmonic excitation strategies in which a second-order harmonic component is introduced to the sinusoidal voltage input with specific phase differences. Subsection 4.1 experimentally investigates the phase-difference-dependent emission enhancement, while Subsection 4.2 analyzes these findings based on the transient results of the simulation. Finally, Section 5 summarizes the key insights and discusses their implications for UV-POCS and other applications that benefit from enhanced ionization at a dielectric surface.

2 Methodology

2.1 Experimental setup

The experimental system is shown in Fig. 2. The atmospheric pressure UV-POCS setup consists of a tungsten electrode with a diameter of 1 mm, a 525-µm-thick undoped silicon chip with a 3 µm oxide layer on top, and a grounded electrode underneath the chip. A combination of a B&K precision 4045B signal generator and a power amplifier is used to power the discharge in an arbitrary waveform at 10 kHz. The electrode features a flat tip with the edge rounded to avoid point discharge, as shown in the enlarged view in Fig. 2. The applied voltage is measured with a high voltage probe, whereas the current is measured with a 100 Ω sampling resistor. Both probes are connected to a PicoScope 3204A oscilloscope. A gas pipe is mounted 3 cm above the discharge gap at an angle. The pipe feeds the discharge with constant helium flow, which will be mixed with air upon arriving at the chip surface. The discharge emission is collected with a UV-compatible microscope objective (MO) and is confined by a UV-compatible lens. An intensified charge-coupled device (ICCD) camera (Hamamatsu C8484-05G) is used to obtain the emission profile. A fixed gain factor of 1 is employed. The signal generator and the ICCD camera are triggered by two TGP110 pulse generators and are gated for a time window of 500 ms and 100 ms, respectively. The pulsing of 500 ms of the AC voltage waveform here aims to minimize the dust accumulation and carbon-based deposition on the chip surface observed under continuous AC excitation. The time sequence is controlled in a way that the exposure of the ICCD camera occurs 200 ms after the onset of the discharge, which means that it is in the middle of a discharge time window. That is to ensure a stabilized voltage output so that the ICCD camera gives repeatable results. The electrode is mounted on a translation stage that moves vertically. The position where the gap spacing d equals 0 is determined by touching the chip surface with the electrode tip. The pixel positions of the ICCD images are then mapped to the real-world coordinates with the measured vertical shift of the stage.

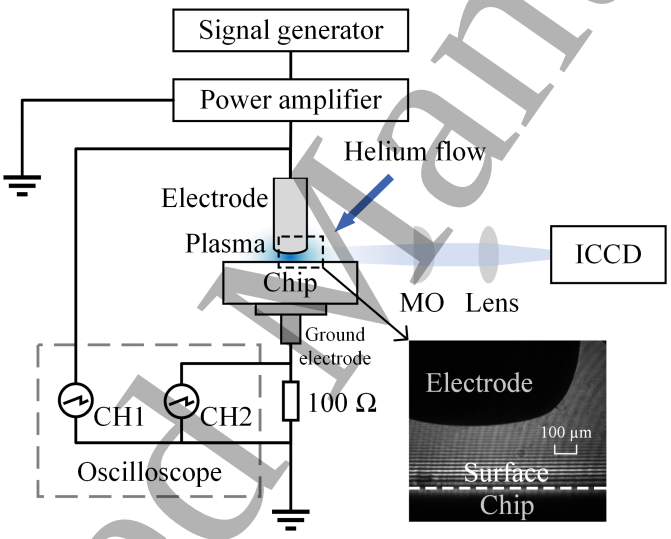

Figure 2: Experimental setup. The enlarged view is an ICCD image that shows the electrode tip profile outlined by a background laser emission at a wavelength of 405 nm.

A pre-test is conducted to determine the helium flow rate used in the experiment. The discharge gap is set to 300 µm, and a 10 kHz sinusoidal voltage input with a peak-to-peak (ptp) amplitude of 3 kV is applied to the tungsten electrode. The emission spectrum is measured horizontally with a 6 mm diameter collimated UV lens placed 3 cm away from the discharge and is analyzed with an AvaSpec 2048 spectrometer. The result is shown in Fig. 3. The first negative system of N_2^+ ($B^2\Sigma_u^+ \rightarrow X^2\Sigma_g^+$) and the second positive system of N_2 ($C^3\Pi_u \rightarrow B^3\Pi_g$) contribute to the majority (in UVA region) of light emission. The strongest line is 391.4 nm, from the first negative system of N_2^+. The percentage of helium in the mixture is varied by controlling the helium flow rate. The correlation between helium mole fraction and helium flow rate is estimated based on CFD simulations (see Supplementary Material). Fig. 4 shows the evolution trend of the longitudinal emission profile (along the centerline of the discharge gap) measured with the ICCD camera with increasing helium flow rate Q. The pixel intensities here are horizontally averaged results over a span of 323 µm, as shown in the inset of Fig. 4. The overall intensity increases along with Q. The intensity drops at both ends of the profile correspond to the sheaths on the chip surface and on the electrode surface (as explained in Fig. 1). The emission in both sheaths saturates at $Q = 4$ SLM. This saturation can be attributed to the gradually weak response of the helium fraction to Q when the latter reaches 4 SLM. Therefore, a baseline operating condition of 4 SLM helium flow rate, 300 µm gap spacing, 10 kHz, and a 3 kV ptp sine wave input is chosen for the convenience of discussion in the following sections.

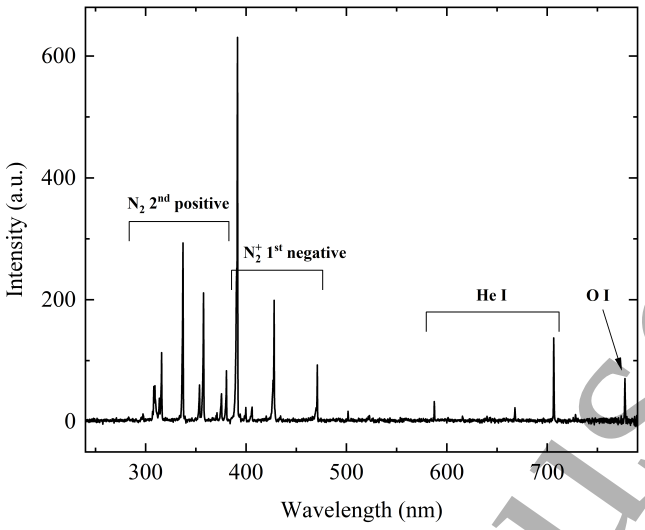

Figure 3: Emission spectrum measured in baseline condition.

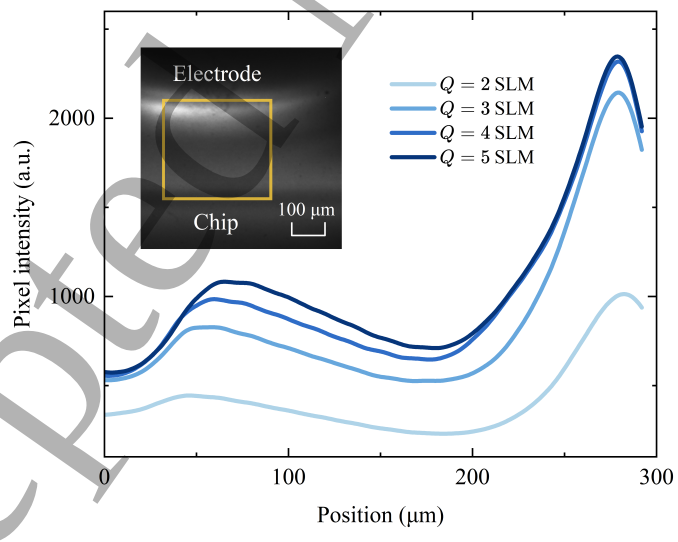

Figure 4: Variation of longitudinal light intensity profile with helium flow rate. The region of interest is located at the center of the discharge setup, marked by the yellow frame. Position 0 corresponds to the chip surface.

2.2 Modeling approach

The model considers a simplified 1D structure in which plasma is generated between the high-voltage electrode and the chip, with the ground electrode underneath the chip. In our experiments, the current peaks induced by microdischarge [15] are present, but they appear infrequently and contribute little to net power consumption in all cases. Thus, the microdischarge is considered unimportant here, and the charge accumulation effect on the chip surface is considered negligible. The chip can then be simplified as an ideal parallel resistor-capacitor (RC) circuit (consideration of the leakage conductance is discussed in the Supplementary Material). The total impedance and the phase angle of the RC circuit used in the model are calculated based on the result of a fast Fourier transform (FFT) analysis of the measured current-voltage (I-V) characteristic of the setup under 3 kV ptp applied voltage.

The baseline operating parameters introduced in Section 2.1 are used as input to the model. Seven species are considered in this study, electrons (e), helium ions (He^+), helium dimer ions (He_2^+), nitrogen molecular ions (N_2^+), nitrogen cluster ions (N_4^+), helium metastable atoms (He^*), and helium dimer metastable atoms (He_2^*). The reaction set considered in this study is given in Table 1. Note that the $N_2^+(B)$ ($B^2\Sigma_u^+$) species is not present in the computation process due to its rapid decay to the ground state through radiative decay R19 and collisional quenching R20. The drift-diffusion assumption is used to compute the number flux and energy flux of all 7 species. The electron mobility and diffusivity are calculated using the Boltzmann solver BOLSIG+ [16] with cross section data from the LXCat database [17, 18] as input. The local energy approximation is applied to compute the mean electron energy, which is used to parameterize the transport and reaction coefficients. The heavy particles have a fixed energy defined by room temperature (300 K) and an initial mole fraction calculated with fluid simulations. The mobility and diffusivity of the heavy particles, as well as the corresponding secondary electron coefficients (SEEC) and the mean initial energy (MIE) of the secondary electron [19, 20, 21] are listed in Table 2.

3 Effect of gap spacing

3.1 Experimental results

To find the optimal geometry that provides enhanced ionization at the chip surface, the emission characteristics of the on-chip plasma are investigated with different gap spacing. The evolution of the emission intensity profile with gaps ranging from 80 µm to 400 µm is shown in Fig. 5. The region of interest is similar to the one used in Fig. 4 and introduced in Section 2.1. As the gap decreases, the light intensity profile shrinks from a 3-layer structure (400 µm case), to a 2-layer structure (300 and 200 µm cases), and eventually a single region with a gap less than 200 µm. The I-V characteristics maintain similar shapes in all cases, indicating that no discharge mode transition occurs. Importantly, the emission intensity on the chip surface increases with thinner gaps. This enhancement is seen to be saturated when the gap is below 100 µm. A reverse trend is noticed with the peak intensity as it decreases when the gap spacing decreases. As a result, the percentage of optical power emitted near the chip surface to the entire gap increased with a smaller gap.

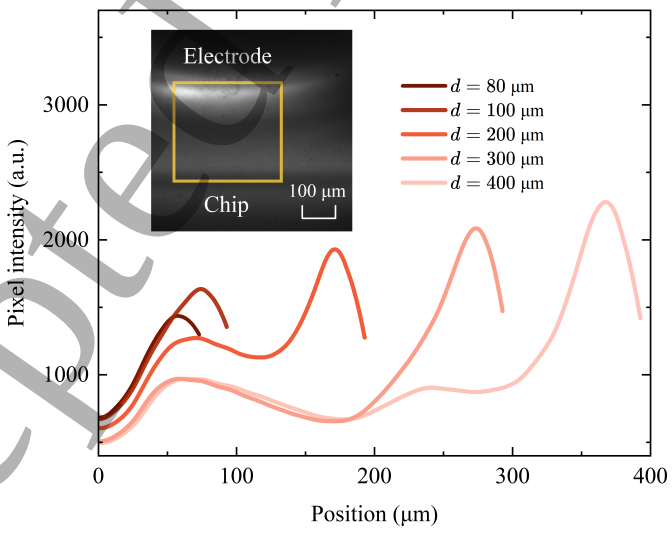

Figure 5: Variation of longitudinal light intensity profile with 4 sets of discharge gap spacing. Position 0 denotes the chip surface. The region of interest here is similar to that used in Fig. 4.

Table 1: Reactions considered in the helium/nitrogen model

Index	Reaction	Rate constant[a]	$\Delta\epsilon_e$[b](eV)	Ref.
	Elastic, ionization, and excitation			
R1	$e + He \rightarrow e + He$	$f(\varepsilon)$		[18]
R2	$e + He \rightarrow e + He^*$	$f(\varepsilon)$	19.8	[18]
R3	$e + He \rightarrow 2e + He^+$	$f(\varepsilon)$	24.6	[18]
R4	$e + He^* \rightarrow 2e + He^+$	$f(\varepsilon)$	4.8	[22]
	Three-body association, metastable pooling, and de-excitation			
R5	$He^* + 2He \rightarrow He_2^* + He$	2×10^{-46}		[23]
R6	$He^+ + 2He \rightarrow He_2^+ + He$	1.4×10^{-43}		[24]
R7	$N_2^+ + N_2 + He \rightarrow N_4^+ + He$	8.9×10^{-42}		[25]
R8	$2He^* \rightarrow e + He_2^+$	2×10^{-15}	-18.2	[24]
R9	$2He^* \rightarrow e + He^+ + He$	8.7×10^{-16}	-15.8	[24]
R10	$He^* + He_2^* \rightarrow e + He^+ + 2He$	5×10^{-16}	-13.5	[26]
R11	$He^* + He_2^* \rightarrow e + He_2^+ + He$	2×10^{-15}	-15.9	[26]
R12	$2He_2^* \rightarrow e + He_2^+ + 2He$	1.2×10^{-15}	-13.7	[26]
R13	$2He_2^* \rightarrow e + He^+ + 3He$	3×10^{-16}	-11.3	[26]
R14	$He_2^* + He \rightarrow 3He$	1.5×10^{-21}		[27]
	Penning ionization and charge exchange			
R15	$He^* + N_2 \rightarrow e + N_2^+(B) + He$	5×10^{-17}	-4.2	[28]
R16	$He_2^* + N_2 \rightarrow e + N_2^+(B) + 2He$	5×10^{-17}	-2.7	[28]
R17	$He^+ + N_2 \rightarrow N_2^+(B) + He$	5×10^{-16}		[29]
R18	$He_2^+ + N_2 \rightarrow N_2^+(B) + 2He$	5×10^{-16}		[29]
	Decay of the excited state			
R19	$N_2^+(B) \xrightarrow{\text{Radiative}} N_2^+ + h\nu$	A		[30]
R20	$N_2^+(B) \xrightarrow{\text{Collisional}} N_2^+$	κA		[30]
	Electron-ion recombination			
R21	$e + He_2^+ + He \rightarrow 3He$	2×10^{-39}		[31]
R22	$e + N_2^+ \rightarrow N_2$	6×10^{-13}		[32]
R23	$e + N_4^+ \rightarrow 2N_2$	2×10^{-12}		[32]

[a] Rate coefficients are in s^{-1}, m^3s^{-1}, and m^6s^{-1}, for single, two, and three body reactions, respectively. $f(\varepsilon)$ stands for the rate constant as a function of mean electron energy calculated by a Boltzmann solver [16] with the corresponding cross section data as input. A is the Einstein coefficient of $N_2^+(B)$. κ is the quenching ratio defined as the ratio of collisional quenching rate to radiative decay rate A.

[b] A Positive sign indicates loss of electron energy, whereas a negative sign stands for energy gain.

Table 2: Mobility μ, diffusivity D, SEEC and MIE of heavy particles

Incident particles	$\mu(m^2/V{\cdot}s)$[a]	$D(m^2/s)$	SEEC	MIE (eV)
He^*		1.89×10^{-3}	0	0
He_2^*		1.28×10^{-3}	0	0
He^+	$f(E/N)$		0.25	5
He_2^+	$f(E/N)$		0.25	5
N_2^+	$f(E/N)$		0.005	3
N_4^+	Estimated from N_2^+		0.005	3

[a] $f(E/N)$ denotes measured μ as a function of reduced electric field.

3.2 Model results and discussion

The model described in Section 2.2 is adopted here to interpret the experimental findings presented in Section 3.1. Since the N_2^+ first negative system dominates the UV emission (Fig. 3), the total emission rate r_{ems} can be estimated with the reaction rate of reaction R19, r_{19}. Reaction R19 is a fast transient process, and its reaction rate is controlled by much slower preceding reactions through which $N_2^+(B)$ is produced, viz. Penning ionization, R15 and R16, and charge exchange, R17 and R18. Therefore, considering also the emission loss due to collisional quenching R20, r_{ems} can be derived from the conservation of $N_2^+(B)$ as

$$r_{ems} \approx r_{19} = \frac{r_{15} + r_{16} + r_{17} + r_{18}}{\kappa + 1}. \quad (1)$$

The κ value is estimated as 23.8 based on the simulated gas mole fraction and is used hereafter. The time-averaged profile of the electron density and r_{ems} as a function of the gap spacing is shown in Fig. 6. Here we reproduce the transition of the emission intensity profile from a 3-layer structure to a single zone (see r_{ems} results) when decreasing the gap from 400 µm to 100 µm, as observed in the experiment (Fig. 5). The peak electron density remains the same when the gap spacing is greater than or equal to 200 µm and starts to drop as the gap becomes thinner than 200 µm. This is an expected result as the applied voltage moves leftward on the helium Paschen curve, entering a region where sustaining a discharge becomes more difficult as the gap narrows [33]. The electron density on the chip surface, however, shows a different trend, as it increases significantly from 200 µm to 100 µm, which is consistent with the surface light emission enhancement observed in the experiment. The computed electron density doesn't correlate exactly with the measured emission intensity, as the latter correlates with the emission rate of the excited species, not directly with the electron density. The density and emission rate profiles in all cases are symmetric, which differs from the experimental results in Fig. 5. That is due to the model considering only a simplified symmetric 1D geometry, while in reality, the plasma expands slightly in the transverse direction, as shown in Fig. 5 inset. The ground electrode is larger compared to the powered electrode, creating a non-zero transverse electric field component, enhancing plasma expansion towards the high electrical field.

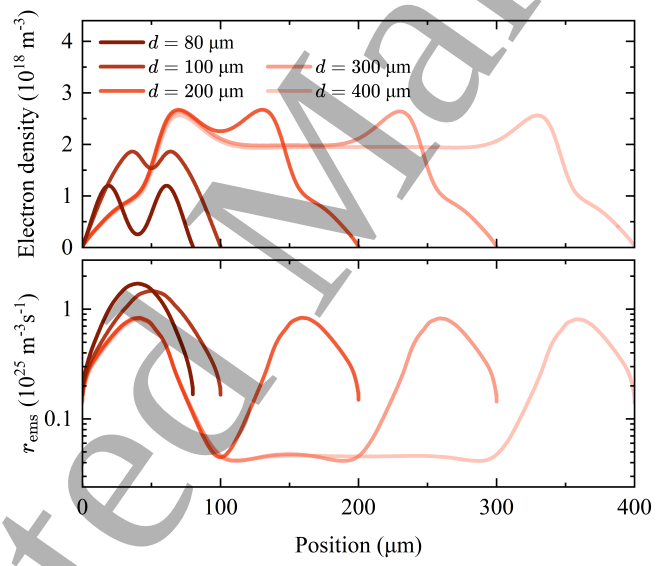

Figure 6: Simulated time-averaged profile of electron density and r_{ems} with different gap spacing. Position 0 denotes the chip surface.

A more detailed comparison of the time-averaged charged particle density in d = 100 µm and d = 300 µm cases is given in Fig. 7. In the d = 300 µm case, there is a quasi-neutral plasma bulk in the center flanked by two sheaths mainly made of ions. However, in the d = 100 µm case, the time-averaged result deviates from the quasi-neutral assumption, as the whole gap becomes positively charged. This rise in time-averaged ion density as the gap spacing decreases is also consistent with the enhanced emission seen in Fig. 6 as a result of the enhanced charge exchange process from helium to nitrogen (R17 and R18). It needs to be pointed out that the charge separation in the time-averaged aspect does not mean that the plasma is completely non-quasi-neutral in both temporal and spatial senses. A detailed explanation will be given at the end of this section with the transient modeling results.

To understand the mechanism behind the collapse of the layered structure, knowledge of the time-resolved processes involved in sustaining the discharge is required. Fig. 8 presents the evolution of the electron density profile within one discharge cycle when d = 300 µm. A similar structure as in the DC glow discharge case [21] is observed, including a cathode sheath that features a drastic drop in electron density, a positive column

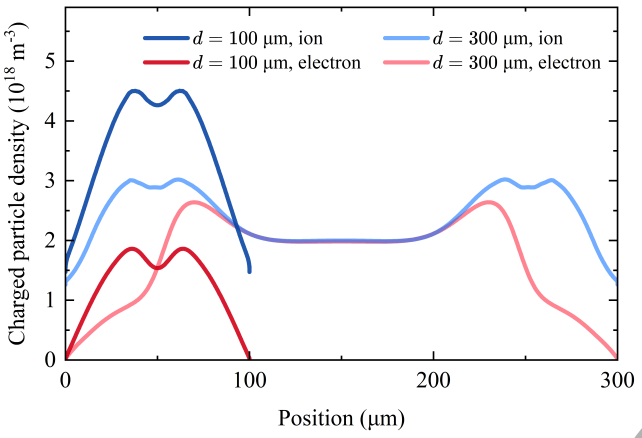

Figure 7: Time-averaged model result of charged particle density profile in d = 100 μm and d = 300 μm cases. Position 0 denotes the chip surface. Electron densities are illustrated with red lines while ion densities are shown in blue.

characterized by a relatively flat profile that occupies most of the gap, and a transition zone connecting both parts, also referred to as a pre-sheath. It is a reasonable analogy, as the discharge is excited with a 10 kHz low-frequency AC source, a frequency much lower than the characteristic frequency of various collisions taking place in the discharge. The electron density peak appears at the sheath edge (or, in the pre-sheath) on the cathode side and is accompanied by a low-density region inside the cathode sheath where electrons have not yet gained sufficient energy from the electric field to ionize. The electrons leaving the sheath are then driven by the electric field toward the temporary anode, forming a region with a more moderate density gradient, termed the positive column.

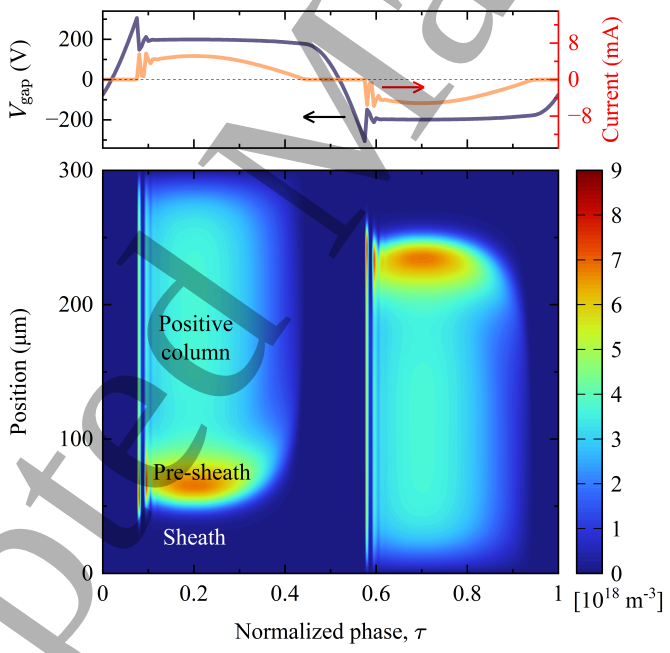

Figure 8: Simulated spatiotemporal distribution of electron density in one discharge period, d = 300 μm. The gap voltage and the discharge current are given as references. Position 0 denotes the chip surface, and the powered electrode is at 300 μm. The phase is adjusted for clarity.

Fig. 9 shows the number densities of all 7 species, the electric potential V, the mean electron energy $\langle \varepsilon_e \rangle$, and the net ionization rate r_{inz} at the current peak phase (τ = 0.2 in Fig. 8), where the chip surface acts as a cathode (position 0). Note that the transient results here take a different shape from Fig. 6 and Fig. 7, as the latter are time average results over one AC cycle. It could be seen that the main potential drop (~170 V) lies in the cathode sheath, where electrons (primary electrons and secondary electrons) gain sufficient energy and start to ionize neutral particles, forming an ionization zone (sheath and part of the pre-sheath). The potential drop in bulk plasma is only ~30 V, which follows the requirement of quasi-neutrality. The He^+ and He_2^+ produced

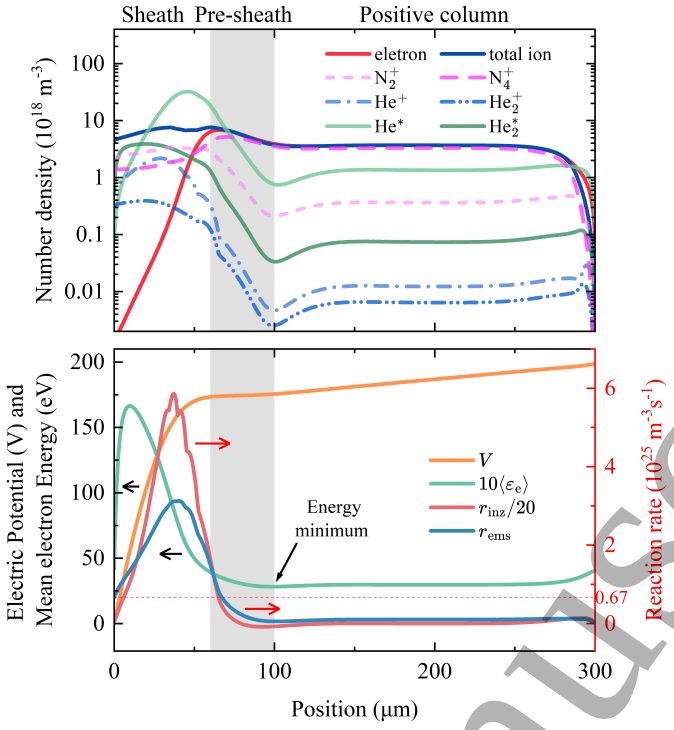

Figure 9: Transient model result of number densities, electric potential V, mean electron energy $\langle\varepsilon_e\rangle$, net ionization rate r_{inz}, and emission rate r_{ems} at $\tau = 0.2$ in $d = 300$ μm case. The values of $\langle\varepsilon_e\rangle$ and r_{inz} are rescaled for clarity. Position 0 denotes the chip surface. The value of r_{ems} at the chip surface is marked with a red dashed line.

in the ionization zone are then trapped inside the sheath potential barrier. They contribute to the major light emission on the chip surface (and the production of N_2^+), as the charge exchange reactions R17 and R18 are more efficient compared to the Penning ionization R15 and R16. The intense ionization inside the cathode sheath is also accompanied by strong excitation of the helium atoms to their metastable state He^* (R2) and the final product He_2^* (R2 + R5). They contribute to the major production of N_2^+ and the subsequent emission process N_2^+ ($B^2\Sigma_u^+ \rightarrow X^2\Sigma_g^+$) in the ionization zone through Penning ionization R15 and R16. Upon leaving the ionization zone, N_2^+ quickly transforms to N_4^+ as the three-body association R7 becomes efficient at atmospheric pressure. The ions inside the sheath contribute to maintaining the discharge by producing secondary electrons. This is similar to the DC glow discharge, where the discharge is sustained with the secondary electron (indicated by the gamma coefficient) and ionization occurs mainly inside the sheath or at the sheath edge [21]. The cathode sheath thickness is ~60 μm, and no sheath structure is found on the anode side. The minimum mean electron energy appears between the pre-sheath and the positive column (~100 μm from the chip surface), resulting in a minimum of r_{ems} at the same position. The time averaging of the transient result of r_{ems} therefore produces a 3-layer structure with two minima present when the temporary cathode and anode switch sides. This is consistent with the time-averaged results in Fig. 6 as a transition from the 2-layer structure to the 3-layer structure occurs when $d > 200$ μm, the requirement for the pre-sheath regions not to overlap in space with each other when flipping the polarity of the electric field.

The result of the $d = 100$ μm case is given for comparison in Fig. 10. Compared to the $d = 300$ μm case, the positive column characterized by the flat densities of all species is not present, leaving only the cathode sheath and the pre-sheath in the gap. The minimum of $\langle\varepsilon_e\rangle$ is present at the same position, which now becomes the anode surface. The peak position of the emission rate r_{ems} is close to the center of the gap, so the time-averaged emission profile becomes a single peak structure, which is consistent with the experimental results (Fig. 5). The sheath is slightly reduced in thickness (by (~4 μm) but now occupies the most space in the gap. That explains the non-quasi-neutral time-averaged results in Fig. 7 since now the sheaths start to overlap in space when the polarity of the voltage flips. The sheath potential drop (~170 V) remains almost unchanged, while sheath thickness decreases by ~4 μm, which directly increases the average electric field by ~25%. Enhanced reduced electric field E/N elevates the mean electron energy and eventually the ionization cross sections and reaction rate [34] due to their exponential dependence on the electron energy [35]. Importantly, the emission rate on the cathode surface is slightly increased as a result of the enhanced ionization and charge exchange reactions (R17 and R18) at the surface. A detailed evaluation on the emission enhancement will be given at the end of Subsection 4.2.

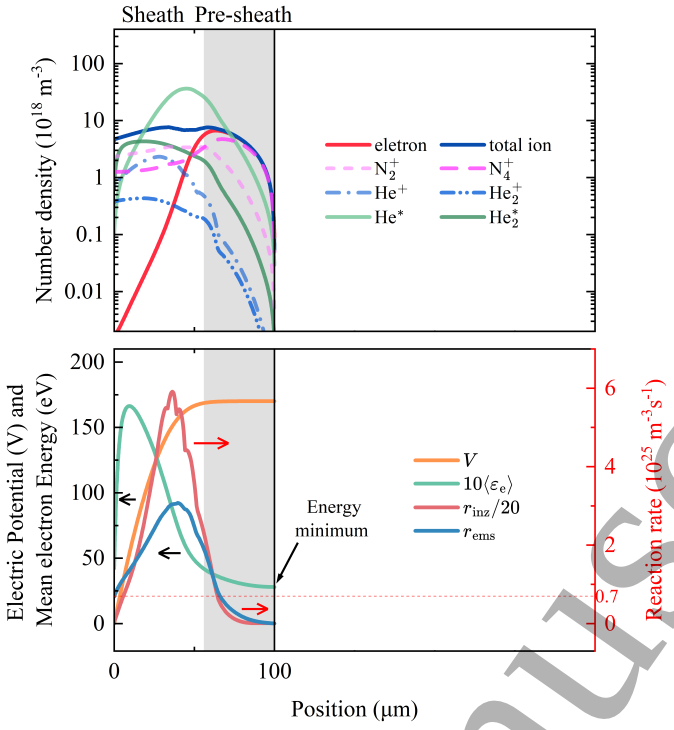

Figure 10: Transient model result of number densities, electric potential V, mean electron energy $\langle\varepsilon_e\rangle$, net ionization rate r_{inz}, and emission rate r_{ems} at $\tau = 0.2$ in $d = 100$ μm case. The values of $\langle\varepsilon_e\rangle$ and r_{inz} are rescaled for clarity. Position 0 denotes the chip surface. The value of r_{ems} at the chip surface is marked with a red dashed line.

4 Harmonic excitation and effect of phase difference

4.1 Experimental results

In addition to optimizing the spatial distribution of the electric field, enhancement of the ionization can be further achieved by modulating the temporal distribution of the applied voltage, namely harmonic excitation. With knowledge of the discharge structure in response to the gap spacing, $d = 300$ μm is chosen for the study of harmonic excitation. This is to guarantee enough space for the response of the transient discharge to the driving waveform to be well observed. The harmonic excitation is implemented by adding a second-order harmonic on the fundamental component while controlling the voltage amplitude to be the same as in the sinusoidal case. The second-order harmonic is attenuated by a factor of 2 to compensate for the difference in capacitive reactance resulting from the frequency difference. The waveform takes the form of

$$V_{in}(t) = \frac{V_0}{C(\phi)}(\sin(2\pi f_0 t) + \frac{1}{2}\sin(4\pi f_0 t + \phi)), \tag{2}$$

where ϕ is the phase difference between the two frequency components, and $C(\phi)$ is a scaling coefficient to ensure $2V_0$ equals the controlled ptp voltage amplitude. The waveforms studied are illustrated in Fig. 11. Note that adding 180° to ϕ (for instance, from 90° to 270°) is equivalent to flipping the waveform across the x-axis (polarity reversal). That is different from simply negating ϕ as the latter flips the waveform across both the x- and y-axes (reversal in both polarity and phase). In the $\phi = 240°$ and $\phi = 270°$ cases, the powered electrode is more positively biased, whereas in the $\phi = 60°$ and $\phi = 90°$ cases, the polarity reverses. Corrections of amplitude and phase are made before feeding the waveform to the signal generator to compensate for the gain difference and phase delay induced by the power amplifier. The I-V characteristic of the setup (using a ptp voltage lower than the onset requirement of discharge) with the harmonic excitation is analyzed through FFT to make sure that the capacitive reactances of the two frequency components are balanced, which is expected by using a coefficient of $\frac{1}{2}$ for the second harmonic term in equation 2.

The response of the emission intensity profile to the variation in the input voltage waveform is shown in Fig. 12. The findings can be summarized as follows.

1. within the investigated range of ϕ, harmonic excitation leads to higher emission intensity than the sine wave;
2. positive polarity ($\phi = 240°$ and $\phi = 270°$) leads to enhanced surface light emission intensity at the chip side, while negative polarity ($\phi = 60°$ and $\phi = 90°$) enhances the powered electrode side;

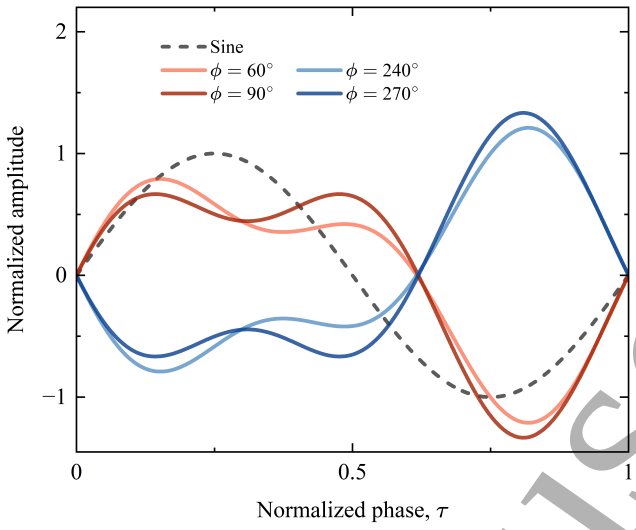

Figure 11: Harmonic excitation waveforms with different phase difference ϕ between the two frequency components. The amplitude is normalized with V_0, and the phases of each waveform are shifted to satisfy the alignment at the origin of coordinates for clear comparison.

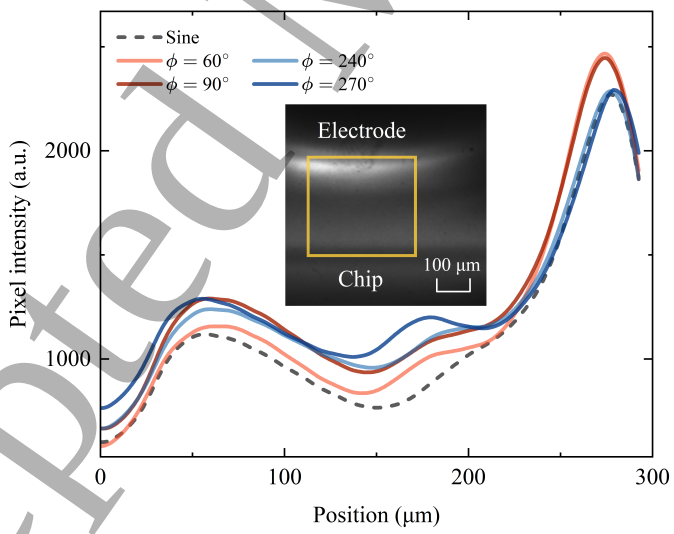

Figure 12: Variation of longitudinal light intensity profile with different phase differences of the harmonic excitation, compared with the sinusoidal case in the same (fundamental) frequency (10 kHz). The latter is illustrated with a dashed line. The positive polarity group ($\phi = 240°$ and $\phi = 270°$) is shown in blue, whereas the negative group ($\phi = 60°$ and $\phi = 90°$) is shown in red. Position 0 denotes the chip surface. The region of interest here is identical to that used in Fig. 4.

3. 270° phase difference gives the most intense emission at the chip surface.

It is also worth noting that in all 4 harmonic excitation cases (d = 300 µm), the emission profile shows a 3-layer structure, similar to the one presented in Fig. 5. As discussed in section 3.2, the appearance of the additional intensity peak in the center is due to the cathode sheaths on both sides becoming spatially separated (see Subsection 3.2). That indicates that the cathode sheath becomes thinner with respect to the discharge gap in the harmonic excitation cases. That is also consistent with the enhanced emission observed on the surface of the anode and cathode (chip surface in $\phi = 90°, 240°, 270°$ cases and powered electrode surface in $\phi = 60°, 90°$ cases).

4.2 Model results and discussion

The observed trends of the emission profile transformation in response to the input waveform are reproduced with the model, as shown with the time-averaged electron density and emission rate in Fig. 13. Within the studied range of ϕ, the introduction of a second-order harmonic component results in a thinner sheath, which means that the plasma is pushed further down toward the anode or the cathode. The polarity of the waveform induces a preference for local enhancement of the discharge: specifically, positive polarity (240° and 270°) tends to enhance the local ionization on the chip surface, while negative polarity (60° and 90°) favors the powered electrode side, consistent with the experimental finding. The 270° phase difference provides the best ionization and emission enhancement on the chip surface.

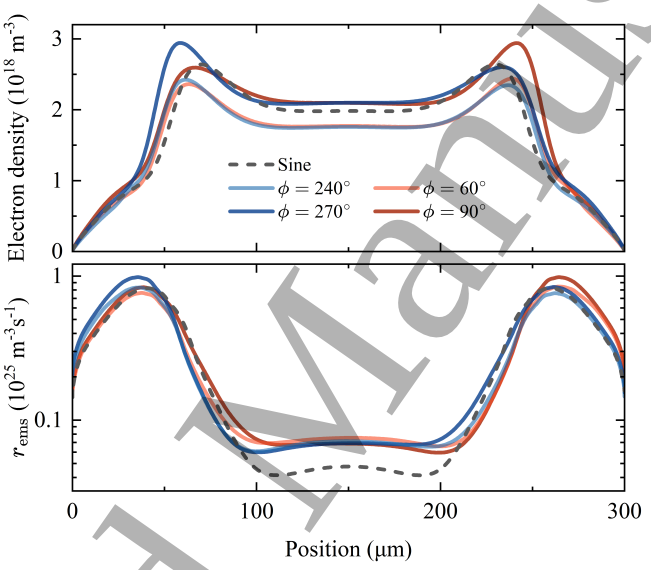

Figure 13: Time-averaged model result of electron density profile's response to the input voltage waveform. Position 0 denotes the chip surface.

The enhancement mechanism can be explained with insight into the evolution of discharge parameters over time. Fig. 14 illustrates the phase-resolved gap voltage, total discharge current, and the ionization source term S_{inz} (total net electron production rate in the entire gap) in response to the input voltage waveform. Compared to the sine wave voltage input case which predicts symmetric results with respect to the x-axis, harmonic excitation with $\phi = 270°$ provides a higher peak gap voltage (~205 V, compared to ~199 V with sine wave input) on both the positive and negative sides. The enhancement of the peak gap voltage on both sides is unequal, as the positive peak runs higher than the negative side. This disparity results in unbalanced responses of the discharge current, with a higher positive peak ($\tau = 0.3$) compared to the negative peak ($\tau = 0.6$). A similar trend is observed with the ionization source term S_{inz}. That is because charge carriers are produced through ionization and S_{inz} is positively correlated with the magnitude of the discharge current. These results indicate that the power deposition in the plasma is redistributed temporally with the harmonic excitation ($\phi = 270°$), and the ionization is enhanced more when the gap is positively biased within one discharge period.

The unevenness in the temporal distribution of the power deposition in plasma also leads to a change in its spatial distribution. Fig. 15 shows the spatial-temporal contour of the electron density. Compared to Fig. 8, where a sine wave input is fed, the overall electron density increases unevenly in the gap. The strongest enhancement occurs around $\tau = 0.3$, where the chip acts as a cathode. The peak electron density appears in the cathode layer and exceeds 1.2×10^{19} m^{-3}. The enhancement on the other side is weaker (for instance, around $\tau = 0.6$ with a peak electron density of 9.6×10^{18} m^{-3}). This spatial preference for enhancement forms the asymmetrical profiles of the time-averaged electron density (Fig. 13).

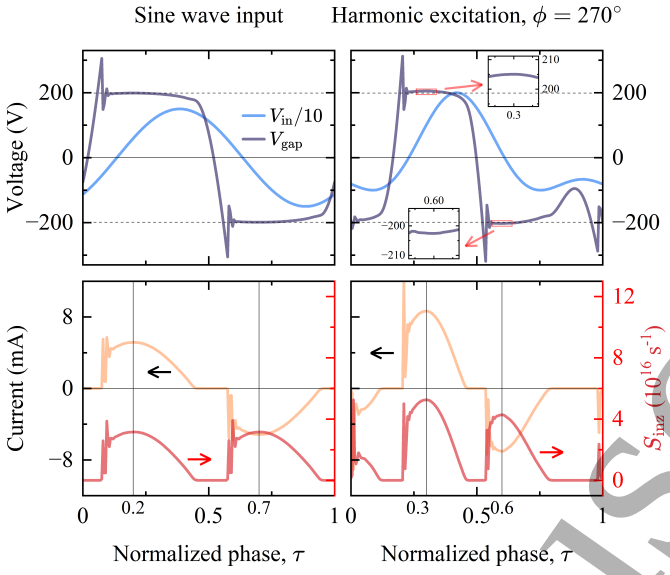

Figure 14: Phase-resolved model result of gap voltage, total discharge current, and ionization source term S_{inz} in both sine wave input case (left column) and harmonic excitation case with $\phi = 270°$ (right column). The scaled input waveforms are given as a reference. The phases are adjusted for clarity. The peak gap voltages of the sine wave input case (symmetric about the x-axis) are marked in both columns with dashed lines. The inserts in the top right image show the enlarged view of the peak gap voltages.

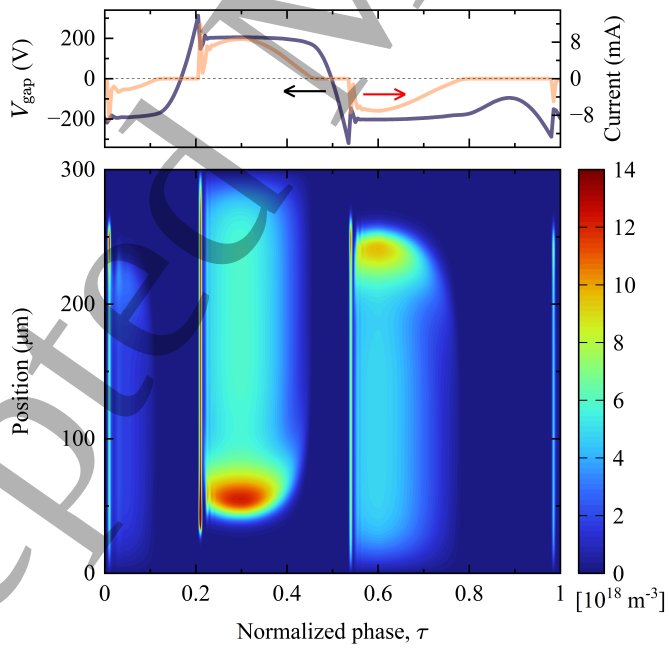

Figure 15: Model result of spatiotemporal distribution of electron density in harmonic excitation case with $\phi = 270°$ and $d = 300$ μm. The gap voltage and the discharge current are given as references. Position 0 denotes the chip surface and the powered electrode sits at 300 μm. The phases are adjusted for clarity, the same way as in Fig. 14.

To conclude the analysis of both the spatial and temporal enhancement effect, we quantitatively evaluate in Fig. 16 the emission enhancement achieved by combining the gap spacing optimization and harmonic excitation. Here we define a surface layer region with a thickness of 3 µm and an area identical to the cross section of the powered electrode, where plasma-wall interactions (such as evanescent wave coupling) take place. The total emission rate in the surface layer $S_{\mathrm{ems,s}}$ is predicted to increase by 12% with a shortened gap and by 48% with both techniques, which is supported by the average pixel intensity in this region measured in the experiment.

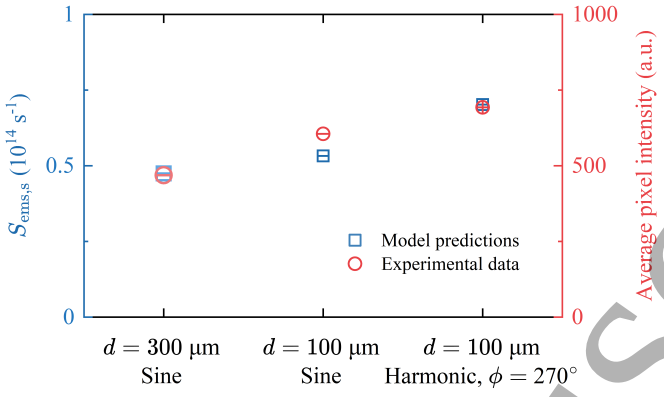

Figure 16: Enhancement of emission in the surface layer predicted by the model and observed in experiments. Model predicted total emission rate $S_{\mathrm{ems,s}}$ (in blue) is the volume integration of emission rate r_{ems}, whereas experimental data (in red) is average pixel intensity in this region.

5 Conclusion

The enhancement of local ionization in micro-gap atmospheric DBD plasma is achieved through both gap spacing optimization (spatial control) and harmonic excitation (temporal control). An enhancement in surface light emission of 48% is achieved using the combined techniques. The 1D plasma model presented in this study successfully reproduced the qualitative trends observed in the experiments, providing insights into the ionization and emission characteristics and sheath dynamics under controlled voltage input.

The experimental and modeling results demonstrated that the reduction of the gap spacing contributes to intensified ionization and emission near the chip surface, resulting from an enhanced electric field in the cathode sheath and the spatial overlap of the sheaths when the voltage polarity flips. Decreasing the gap to an extent where the spacing is less than twice the thickness of the cathode sheath leads to an increased emission intensity on the chip surface, as predicted by the model.

Introducing a second-order harmonic component to sinusoidal excitation, namely harmonic excitation, further enhances the emission intensity on the chip surface, in particular with a phase difference of 270°. Experimental results under harmonic excitation indicate that the sheath undergoes thinning, leading to plasma confinement closer to the chip surface, as validated by the model. Additionally, this improvement comes with a waveform-dependent spatial selectivity, specifically, a positive polarity favors the dielectric side and a negative polarity favors the powered electrode side. The mechanism behind this improvement lies in the amplification of the peak gap voltages, which leads to a temporal redistribution of power deposition.

Together, these findings establish a methodology for the realization of UV-POCS and provide practical guidance for optimizing atmospheric-pressure microplasmas. Such advances are particularly beneficial for applications that require localized ionization control, including surface activation, chemical synthesis, and biomedical device fabrication.

Acknowledgment

The authors would like to thank Ghent University for its financial support via the Special Research Fund (BOF-IOP) under Grant 01IO1320. The work of Nicolas Le Thomas was also supported by the FWO research project Weave under Grant G033722N.

References

[1] Joseph R Lakowicz. Principles of fluorescence spectroscopy. Springer, 2006. DOI: 10.1007/978-0-387-46312-4.

[2] Chupao Lin et al. UV photonic integrated circuits for far-field structured illumination autofluorescence microscopy. *Nature communications* 13.1 (2022), 4360. DOI: 10.1038/s41467-022-31989-8.

[3] Chupao Lin, Yujie Guo, and Nicolas Le Thomas. Demonstration of a photonic integrated circuit for quantitative phase imaging. *Photonics Research* 13.1 (2024), 1–17. DOI: 10.1364/PRJ.523534.

[4] Chenming Su et al. Low-loss and high-index contrast ultraviolet-C free-standing waveguides made of thermal silicon oxide. *Optics letters* 49.13 (2024), 3785–3788. DOI: 10.1364/OL.530364.

[5] S-J Park et al. W of average power at 172 nm in the vacuum ultraviolet from flat, efficient lamps driven by interlaced arrays of microcavity plasmas. *Apl Photonics* 2.4 (2017). DOI: 10.1063/1.4976530.

[6] Kai Zoschke et al. Hermetic wafer level packaging of MEMS components using through silicon via and wafer to wafer bonding technologies. *IEEE 63rd Electronic Components and Technology Conference*. IEEE, 1500–1507. DOI: 10.1109/ECTC.2013.6575770.

[7] Werner Siemens. Ueber die elektrostatische Induction und die Verz¨ogerung des Stroms in Flaschendr¨ahten. *Annalen der Physik* 178.9 (1857), 66–122. DOI: 10.1002/andp.18571780905.

[8] Ulrich Kogelschatz. Dielectric-barrier discharges: their history, discharge physics, and industrial applications. *Plasma chemistry and plasma processing* 23.1 (2003), 1–46. DOI: 10.1023/a:1022470901385.

[9] Fran¸coise Massines et al. Recent advances in the understanding of homogeneous dielectric barrier discharges. *The European Physical Journal-Applied Physics* 47.2 (2009), 22805. DOI: 10.1051/epjap/2009064.

[10] Daniel M Sherman. The transition from a filamentary dielectric barrier discharge to a diffuse barrier discharge in air at atmospheric pressure. *Journal of Physics D: Applied Physics* 38.4 (2005), 547. DOI: 10.1088/0022-3727/38/4/006.

[11] Francis Chen. Introduction to plasma physics and controlled fusion. Springer, 2015. DOI: 10.1007/978-3-319-22309-4.

[12] Ronny Brandenburg et al. The transition between different modes of barrier discharges at atmospheric pressure. *Journal of Physics D: Applied Physics* 42.8 (2009), 085208. DOI: 10.1088/0022-3727/42/8/085208.

[13] Ihor Korolov et al. Helium metastable species generation in atmospheric pressure RF plasma jets driven by tailored voltage waveforms in mixtures of He and N2. *Journal of Physics D: Applied Physics* 53.18 (2020), 185201. DOI: 10.1088/1361-6463/ab6d97.

[14] ZL Zhang et al. Ionization asymmetry effects on the properties modulation of atmospheric pressure dielectric barrier discharge sustained by tailored voltage waveforms. *Physics of Plasmas* 25.4 (2018). DOI: 10.1063/1.5020216.

[15] Ulrich Kogelschatz, Baldur Eliasson, and W Egli. Dielectric-barrier discharges. Principle and applications. *Le Journal de Physique IV* 7.C4 (1997), C4–47–C4–66. DOI: 10.1051/jp4:1997405.

[16] GJM Hagelaar and L C Pitchford. Solving the Boltzmann equation to obtain electron transport coefficients and rate coefficients for fluid models. *Plasma sources science and technology* 14.4 (2005), 722. DOI: 10.1088/0963-0252/14/4/011.

[17] Itikawa database. Online Database. Retrieved on February 11, 2025. URL: www.lxcat.net.

[18] S.F. Biagi Fortran program MAGBOLTZ 8.97. Online Database. Retrieved on February 11, 2025. URL: www.lxcat.net.

[19] HW Ellis et al. Transport properties of gaseous ions over a wide energy range. *Atomic data and nuclear data tables* 17.3 (1976), 177–210. DOI: 10.1016/0092-640X(76)90001-2.

[20] Edward N Fuller, Paul D Schettler, and J Calvin Giddings. New method for prediction of binary gas-phase diffusion coefficients. *Industrial & Engineering Chemistry* 58.5 (1966), 18–27. DOI: 10.1021/ie50677a007.

[21] Boris M Smirnov. Theory of gas discharge plasma. Vol. 84. Springer, 2015. DOI: 10.1007/978-3-319-11065-3.

[22] TRINITI database. Online Database. Retrieved on February 11, 2025. URL: www.lxcat.net.

[23] Yu B Golubovskii et al. Modelling of the homogeneous barrier discharge in helium at atmospheric pressure. *Journal of Physics D: Applied Physics* 36.1 (2002), 39. DOI: 10.1088/0022-3727/36/1/306.

[24] Qiang Wang, Demetre J Economou, and Vincent M Donnelly. Simulation of a direct current microplasma discharge in helium at atmospheric pressure. *Journal of Applied Physics* 100.2 (2006). DOI: 10.1063/1.2214591.

[25] GM Petrov et al. Numerical modeling of a He–N2 capillary surface wave discharge at atmospheric pressure. *Plasma Chemistry and Plasma Processing* 20 (2000), 183–207. DOI: 10.1023/A:1007065022725.

[26] R Deloche et al. High-pressure helium afterglow at room temperature. *Physical Review A* 13.3 (1976), 1140. DOI: 10.1103/PhysRevA.13.1140.

[27] TJ Millar, PRA Farquhar, and K Willacy. The UMIST database for astrochemistry 1995. *Astronomy and Astrophysics Supplement Series* 121.1 (1997), 139–185. DOI: 10.1051/aas:1997118.

[28] MA Lieberman. Analytical model of atmospheric pressure, helium/trace gas radio-frequency capacitive Penning discharges. *Plasma Sources Science and Technology* 24.2 (2015), 025009. DOI: 10.1088/0963-0252/24/2/025009.

[29] Xiaohui Yuan and Laxminarayan L Raja. Computational study of capacitively coupled high-pressure glow discharges in helium. *IEEE Transactions on Plasma Science* 31.4 (2003), 495–503. DOI: 10.1109/TPS.2003.815479.

[30] Olfa Ferchichi et al. Accurate Einstein coefficients for electric dipole transitions in the first negative band of N2+. *Astronomy & Astrophysics* 661 (2022), A132. DOI: 10.1051/0004-6361/202142869.

[31] KR Stalder et al. Modeling the chemical kinetics of high-pressure glow discharges in mixtures of helium with real air. *Journal of applied physics* 99.9 (2006). DOI: 10.1063/1.2193170.

[32] WH Kasner, WA Rogers, and MA Biondi. Electron-ion recombination coefficients in nitrogen and in oxygen. *Physical Review Letters* 7.8 (1961), 321. DOI: 10.1103/PhysRevLett.7.321.

[33] Leonid Babich and V Loˇıko Tat'yana. Generalized Paschen's law for overvoltage conditions. *IEEE Transactions on Plasma Science* 44.12 (2016), 3243–3248. DOI: 10.1109/TPS.2016.2629022.

[34] Allan J Lichtenberg. Principles of plasma discharges and materials processing. Wiley-Interscience, 2005. DOI: 10.1002/0471724254.

[35] Alexander Fridman. Plasma chemistry. Cambridge university press, 2008. DOI: 10.1017/CBO9780511546075.